Effect of MgO content on the quantitative role of hydrotalcite-like phase in a cement-slag system during carbonation

Zhang, Yu; Liang, Minfei; Gan, Yidong; Çopuroğlu, Oğuzhan

DOI
10.1016/j.cemconcomp.2022.104765

Publication date
2022

Document Version
Final published version

Published in
Cement and Concrete Composites

Cement and Concrete Composites 134 (2022) 104765

Contents lists available at ScienceDirect

Cement and Concrete Composites

journal homepage: www.elsevier.com/locate/cemconcomp

Effect of MgO content on the quantitative role of hydrotalcite-like phase in a cement-slag system during carbonation

Yu Zhang *, Minfei Liang, Yidong Gan, Oğuzhan Çopuroğlu

Microlab, Section Materials and Environment, Faculty of Civil Engineering and Geosciences, Delft University of Technology, Delft, the Netherlands

ARTICLE INFO

Keywords:
Cement-slag system
MgO
Hydrotalcite-like phase
Carbonation
Thermodynamic modelling

ABSTRACT

This paper reports the carbonation characteristics of a cement-slag system exposed to accelerated carbonation testing, and its improved carbonation resistance with the increasing MgO content in blast furnace slag, in which hydrotalcite-like phase plays a key role.

Our research showed that the hydrotalcite-like phase started to carbonate upon contacting with the carbonate ions and bound more than 15 wt% CO_3^{2-} in the mildly carbonated and transition areas. This value was positively associated with the magnesia content of slag. Additionally, the proportion shared by hydrotalcite-like phase decreased in the fully carbonated area, and more CO_2 was fixed in the form of calcium carbonate. Consistent with the thermodynamic modelling, the ratio of CO_2 bound in carbonated hydrotalcite-like phase to the total $CaCO_3$ continued to decrease as the CO_2 ingress progressed. On the other hand, the reaction between hydrotalcite-like phase and CO_2 was found to be volumetrically stable due to binding CO_2 in the interlayer space, and Mg was still distributed within the original slag grain region. Mg/Al atomic ratio of hydrotalcite-like phase remained nearly the same before and after carbonation. Results of this study quantitatively emphasized the favorable effect of hydrotalcite-like phase to improve the carbonation resistance of slag-rich cementitious systems.

1. Introduction

Blast furnace slag (henceforth *slag*) is the by-product of pig iron production. It is generally assumed that for every ton of pig iron produced, the slag output is about 0.2 ton [1]. In the furnace, molten slag formed from flux agent, coke ash, and residue of iron ore between 1400 and 1600 °C floats on top of molten iron liquid and can be expressed as a $CaO–SiO_2–Al_2O_3–MgO$ system. Through rapid cooling, more than 90% of the water-quenched slag contains a glassy phase, which possesses latent hydraulic properties. Therefore, it is mostly used as supplementary cementitious material (SCM) in the cement industry. However, due to the heterogeneity of the raw materials fed into the furnace, the production technology and standard formulation, the chemical composition and property of slag varies -as an end product-from location to location. Questions regarding the effect of slag components on the evolution of phase assemblages, microstructure development and durability of cement-slag systems are of great interest. Therefore, a further insight into slag chemistry should help design slag contributing to constructing high-performance slag–rich concrete structures.

Generally, the amount of MgO in European slag varies from approximately 0 to 17 wt%, according to Refs. [2,3]. Based on [4,5], it was in the range of 5–15 wt% in North America. The MgO content of slag produced in Austria was a little lower, typically ≤10 wt% [6]. In fact, the MgO content of slag was directly related to the composition of flux agent (essentially limestone and dolomite) added into the furnace, which was matched to the melting rate of iron ore in order to achieve a lower melting point, thin-bodied and iron-free blast furnace slag [1]. However, to lower the liquidus temperature of molten phase for metallurgical reasons [7–9], increasing the amount of limestone over dolomitic rocks have been preferred, leading to the emerging trend that only lime-rich and magnesium-poor slag has been produced and used in cement production. There is evidence that this trend has affected the cement quality, particularly concerning carbonation related surface durability issues [10].

In the network structure of slag, Mg^{2+} ion with smaller radius tends to act as a network modifier. Gradual addition of MgO in slag will react with the bridging oxygen (BO) of silicate network, producing non-bridging oxygen (NBO). There is a common consensus existing that the field strength of cation, represented by z/r^2 (z and r being the charge and radius of the cation, respectively.), reveals the strength of the bond

* Corresponding author.
E-mail addresses: Y.Zhang-28@tudelft.nl (Y. Zhang), M.Liang-1@tudelft.nl (M. Liang), Y.Gan@tudelft.nl (Y. Gan), O.Copuroglu@tudelft.nl (O. Çopuroğlu).

https://doi.org/10.1016/j.cemconcomp.2022.104765
Received 4 July 2022; Received in revised form 4 September 2022; Accepted 10 September 2022
Available online 16 September 2022

between a non-bridging oxygen and a cation. A cation with larger z/r^2 tends to generate a more depolymerized structure [11]. The field strength of cation is commonly observed in slag following the order: $K^+ < Na^+ < Ca^{2+} < Mg^{2+}$ [12]. Therefore, results from Refs. [13,14] concluded that magnesium in slag presented stronger capability to break the linkage of silicate network structure. The works in Ref. [15] confirmed that when substituted with Ca and Mg, an increased distortion of network structure was observed. With the increasing of MgO + CaO content, the network depolymerization and thus the glass reactivity increased correspondingly, which was consistent with the results in Ref. [16]. According to the European standard EN 15167-1, it is required that $(CaO + MgO)/SiO_2 > 1$, which means that the effect of MgO in slag is considered similar to that of CaO, and a deficiency in one component could be compensated by the other. From this perspective, the gradual change in slag composition mentioned earlier (i.e., lime-rich and magnesium-poor slag) should not impose any adverse effect on its engineering properties.

In the past decade much more effort has been devoted to investigating the effect of MgO content of slag on the evolution of phase assemblages of alkali-activated slag (AAS) systems [17–20]. Some common conclusions identified were: gradual increase of MgO content in slag increases the amount of hydrotalcite-like phase formed and lowers the aluminum content uptake by C–S–H gel phase. However, to the best of authors' knowledge, few investigations went deep into the correlation between slag chemistry and durability characteristics of slag-containing cementitious systems. The works in Refs. [21,22] confirmed that the formation of hydrotalcite-like phase could reduce the susceptibility to carbonation of AAS produced with higher MgO content, as it appeared to act as an internal CO_2 sorbent. Results in Ref. [23] revealed that a higher MgO content slag precursor for AAS had shown higher resistance to accelerated carbonation-induced degradation due to the improvement in the resistance to gel decalcification and capillary pore formation during carbonation. Questions, such as whether the observations on the AAS systems could be extended to slag-rich cement systems directly remain to be addressed. Meanwhile, researchers recognize the beneficial effect of hydrotalcite-like phase during carbonation; however, most analysis is qualitative. Therefore, understanding the effect of hydrotalcite-like phase quantitatively during carbonation is vital towards achieving the full potential of slag performance in concrete.

Thus, the present study was designed to study the effect of MgO content of slag on the carbonation characteristics of cement-slag system where slag is used as a primary SCM (70 wt% replacement in the paper to simulate CEM III/B). To avoid the interference from other factors, synthetic slags with different MgO contents manufactured in the laboratory were used to produce the cement-slag systems. The phase assemblage, microstructure, and micro-mechanical properties of each mixture before and after accelerated carbonation testing were compared. Through quantitative analysis of hydrotalcite-like phase, the effect of MgO content in slag on carbonation characteristics was determined.

2. Material and methodology

2.1. Materials and mix design

CEM I 42,5 N (manufactured by ENCI Maastricht B.V.) was used to produce the cement-slag systems. Synthetic slags with different MgO contents (M0, M8, and M16) were produced in the laboratory. Details of the production process is given elsewhere [16]. Note that for the production of synthetic slag M0, only analytical reagents (CaO, SiO_2, and Al_2O_3) were added according to the compositional design target, while for slag M8 and M16, analytical reagents and commercial slag were added.

Chemical compositions of the binder components were determined by X-ray fluorescence (XRF) and their particle size distribution (PSD) by laser diffraction, shown in Table 1 and Fig. 1, respectively. Table 2 gives the rough mineralogical composition of the cement clinker based on Bouge calculation. For synthetic slag M0, M8, and M16, their CaO/SiO_2 ratio was kept at around 1 (In fact, for commercial slag with different MgO contents, the CaO/SiO_2 ratio varies; however, this ratio fluctuates around 1.0, e.g., as exhibited in Ref. [2].) and the amount of Al_2O_3 fluctuated at about 14 wt%, while MgO content varied from 0.33 (for M0) to 16.07 wt% (for M16). Quartz (Qz) with a similar PSD was also introduced to cast a cement-quartz sample, acting as a reference.

X-ray diffraction (XRD) measurements of synthetic slag M0, M8 and M16 are illustrated in Fig. 2, which were almost entirely amorphous indicating the non-existence of crystalline phases. It was also noted that the position of amorphous hump shifted slightly to the right with the gradual addition of MgO in slag.

2.2. Methodology

To produce the blends, cement was partially replaced by slag and quartz at a constant substitution level of 70 wt%. The paste mixtures were prepared using a water to binder ratio of 0.40 and cast in cylindrical plastic containers of 20 mL, which were sealed with thin para film to prevent further ingress of CO_2 and evaporation of mixing water. All specimens were stored at 20 ± 3 °C until further use.

After 3 months of curing, specimens of each mixture were taken out of the plastic bottles, the top surface (~5 mm) of which were removed after demoulding. Before transferring them to the carbonation chamber, they were conditioned for one month in a relative humidity (RH)-controlled climate chamber at 65% and 20 °C for pretreatment. Only the freshly cut surfaces were exposed to CO_2 and the other surfaces were sealed to ensure one dimensional gas penetration. Accelerated carbonation testing was performed in a carbonation chamber with regulated CO_2 concentration of 3% ± 0.2, at 20 ± 3 °C and 65 ± 5% of RH (using saturated $NaNO_2$ solution). The total duration of carbonation was up to 6 months.

After the designated hydration and carbonation period, small discs were sawn from the specimens, crushed and immersed in isopropanol solution to exchange the available pore solution. Prior to XRD measurement and thermogravimetric analysis (TGA), the crushed slices were dried at 40 °C, ground with mortar and pestle and sieved manually to obtain particles with diameter below 63 μm. XRD data was collected

Table 1
Chemical compositions (wt.%) and selected physical properties of CEM I 42,5 N and three synthetic slags.

	Cement	M0	M8	M16
CaO	64	43.16	37.04	34.09
SiO_2	20	42.99	37.79	32.99
Al_2O_3	5	13.30	14.51	15.05
MgO	–	***0.33***	***8.83***	***16.07***
FeO/Fe_2O_3	3	0.07	0.28	0.34
TiO2	–	–	0.70	0.73
MnO/Mn_2O_3	–	–	0.17	0.16
Na_2O_{eq}[a]	0.58	–	0.40	0.36
SO_3	2.93	0.01	0.01	0.01
Residual	4.49	0.14	0.18	0.13
CaO/SiO_2	–	1.00	0.98	1.03
$(CaO + MgO)/SiO_2$[b]	–	1.01	1.21	1.52
Physical properties				
d_{50} (μm)[c]	26.81	24.35	22.73	22.29
SSA (m^2/g)[d]	0.284	0.770	0.895	0.964

[a] The Na_2O_{eq} employed here for cement and slag was identical, namely $Na_2O + 0.658*K_2O$.
[b] The European Standard EN 15167-1 recommends that this ratio should be greater than 1.
[c] The particle size distribution of slag was measured by EyeTech, Ankersmid. The d_{50} of quartz was 24.21 μm.
[d] The specific surface area (SSA) of cement and slag was measured by Blaine and nitrogen adsorption with the BET method, respectively.

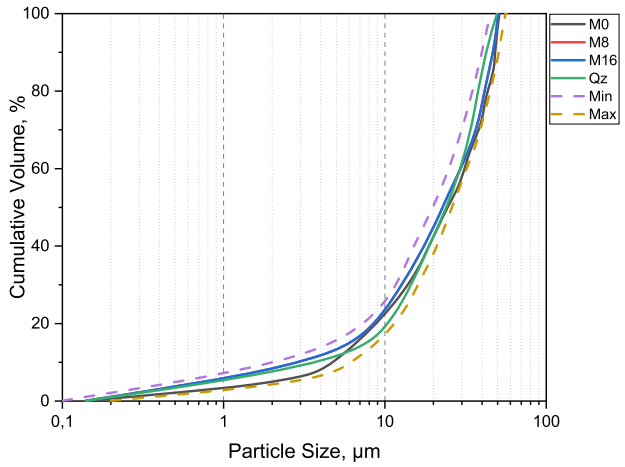

Fig. 1. Particle size distribution of three synthetic slags and quartz.

Table 2
Mineralogical composition (wt.%) of CEM I 42.5 N

Phase	
C_3S	62.24
β-C_2S	10.47
C_3A	8.18
C_4AF	9.12
Gypsum	4.98
Other	5.01

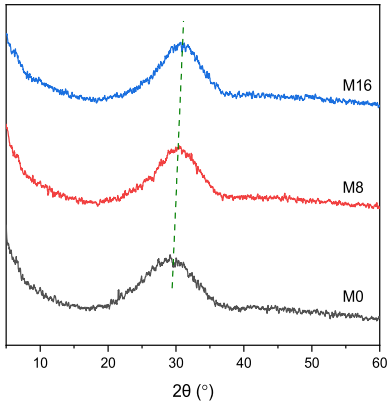

Fig. 2. XRD scans of three synthetic slags used in the present research.

using a Philips PW 1830/40 Powder diffractometer with Cu K-alpha radiation. The machine was operated with an X-ray beam current of 40 mA and an acceleration voltage of 40 kV. Sample powders were scanned from 5 to 60° (2θ) with a step size of 0.03°. Netzsch STA 449 F3 Jupiter coupled with mass spectrometer (MS) Netzsch QMS 430C was employed for thermogravimetric analysis. The emissions of H_2O and CO_2 were thus identified. Approximately 50 mg powder samples were heated under an argon atmosphere at a heating rate of 10 °C/min from 40 to 900 °C in an Al_2O_3 crucible, with an identical and blank crucible as reference. Moreover, the CO_2 response of the samples with unknown CO_2 concentration was calibrated with the response of a standard with known CO_2 concentration (pure agent $CaCO_3$ provided by VWR Chemicals BDH) under the same analytical conditions. This method allowed the quantification of CO_2 emission from carbonated slag cement paste containing both calcium carbonate and other CO_2-bearing phases. The area under the MS CO_2 curve, or the peak integral, was calculated with commercial software OriginPro 2019.

Fourier transform infrared spectroscopy (FTIR) was performed using Spectrum TM 100 Optical ATR-FTIR spectrometer over the wavelength range from 600 to 4000 cm^{-1} to characterize the alteration of molecule structure before and after accelerated carbonation test. A single-beam configuration was used, and each sample was scanned 20 times with a fixed instrument resolution of 4 cm^{-1}.

Mercury intrusion porosimetry (MIP) analysis was carried out on small paste samples. The relationship between pore diameter (D) and pore pressure (P) is given in Washburn equation as the following formula shows,

$$P = -\frac{4\gamma cos(\theta)}{D}$$

of which the surface tension of mercury (γ) is 0.485 N/m at 25 °C and the contact angle between mercury and specimen (θ) is 140°. Three steps were involved in each measurement process, i.e., mercury intrusion at low pressure from 0 to 0.170 MPa; at high pressure from 0.170 to 210 MPa; and mercury extrusion. According to the equation above, the maximum pressure achieved by the equipment corresponded to a minimal pore diameter of about 7 nm, based on a cylindrical pore model. Therefore, pores below this size cannot be detected.

Scanning electron microscopy (SEM) investigation was performed on selected samples, which had been dried at 40 °C, vacuum impregnated with epoxy resin, ground and polished down to 0.25 μm, and carbon coated. The coated samples were examined with FEI QUANTA FEG 650 ESEM at 10 kV accelerating voltage, 10 mm working distance and in backscattered secondary electron (BSE) imaging mode. Energy dispersive X-ray spectroscopy (EDS) point analysis was also used to determine the elemental composition of the phase assemblages observed in the matrix and slag rim.

To obtain the micro-mechanical properties, i.e., modulus of elasticity and hardness, of slag cement paste before and after the accelerated carbonation testing, nanoindentation performed with Agilent Nano Indenter G200 (Keysight, Santa Rosa, CA, USA) equipped with a berkovich tip was used. Two or three randomly chosen areas were selected and around 800 nanoindents were made on each sample. The distance between individual indents was 40 μm.

Thermodynamic modelling was carried out using the Gibbs free energy minimization software GEMS [24,25] with thermodynamic data from the PSI-GEMS database [26,27] supplemented by cement specific data [28,29]. The calcium-alkali aluminosilicate hydrate ideal solid solution model (CNASH_ss) proposed by Myers et al. [30] was employed to describe the C–S(A)−H gel phase in the system. MgAl–OH−LDH_ss containing three end-members with Mg/Al atomic ratios of 2, 3 and 4 reformulated into an ideal solid solution was employed to simulate the formation of hydrotalcite–like phase before carbonation [31]. For their corresponding carbonate forms, the database provided by Ref. [32] was incorporated in the model as candidate phases. The thermodynamic properties of these carbonate forms were calculated based on the ion-exchange constant provided by Ref. [33].

3. Results

3.1. Phenolphthalein spray

The typical cross-sectional surfaces of the specimens after phenolphthalein spray are shown in Fig. 3. It was noted that the carbonation depth decreased significantly with the increasing MgO content in slag, from more than 20 mm for slag M0 paste reduced to approximately 5 mm for slag M16 paste.

3.2. Carbonation products

In this section, the authors characterized the carbonation products of slag cement paste by means of a series of analytical techniques. Powders

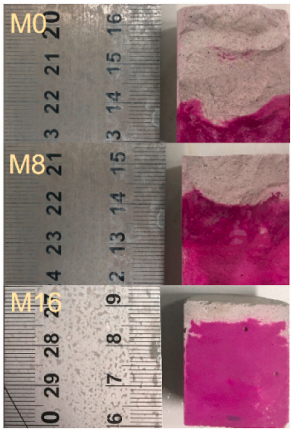

Fig. 3. Typical sawn surfaces of the specimens after spraying with phenolphthalein solution.

used for tests were extracted within the 3 mm depth from the surface of the specimens exposed in the carbonation chamber to ensure the analysis of fully carbonated microstructure.

3.2.1. TG-DTG-MS

TG-DTG results of cement-slag and -quartz mixtures after 3 months of curing are shown in Fig. 4 (a). The highest hydrotalcite-like phase content was detected in slag M16 mixture with a shoulder and a distinct peak located at approximately 250 and 350 °C, respectively. Conversely, there was no hydrotalcite-like phase observed in slag M0 mixture as negligible MgO was available in slag M0. The broad peak at 100–150 °C suggested the presence of C–S–H gel phase. The shoulder at ~200 °C indicated the formation of calcium monosulfoaluminate (monosulfate), sourced from the transformation of ettringite with time.

The DTG results, H_2O and CO_2 MS curves of fully carbonated cement-slag M0, M8, M16, and Qz pastes are plotted in Fig. 4 (b-1)-(b-4), respectively. The main CO_2-bearing phase in cement-Qz paste after carbonation was calcium carbonate, and three decomposition peaks starting from 500 °C in the DTG graph implied the presence of amorphous calcium carbonate, aragonite and/or vaterite, and calcite

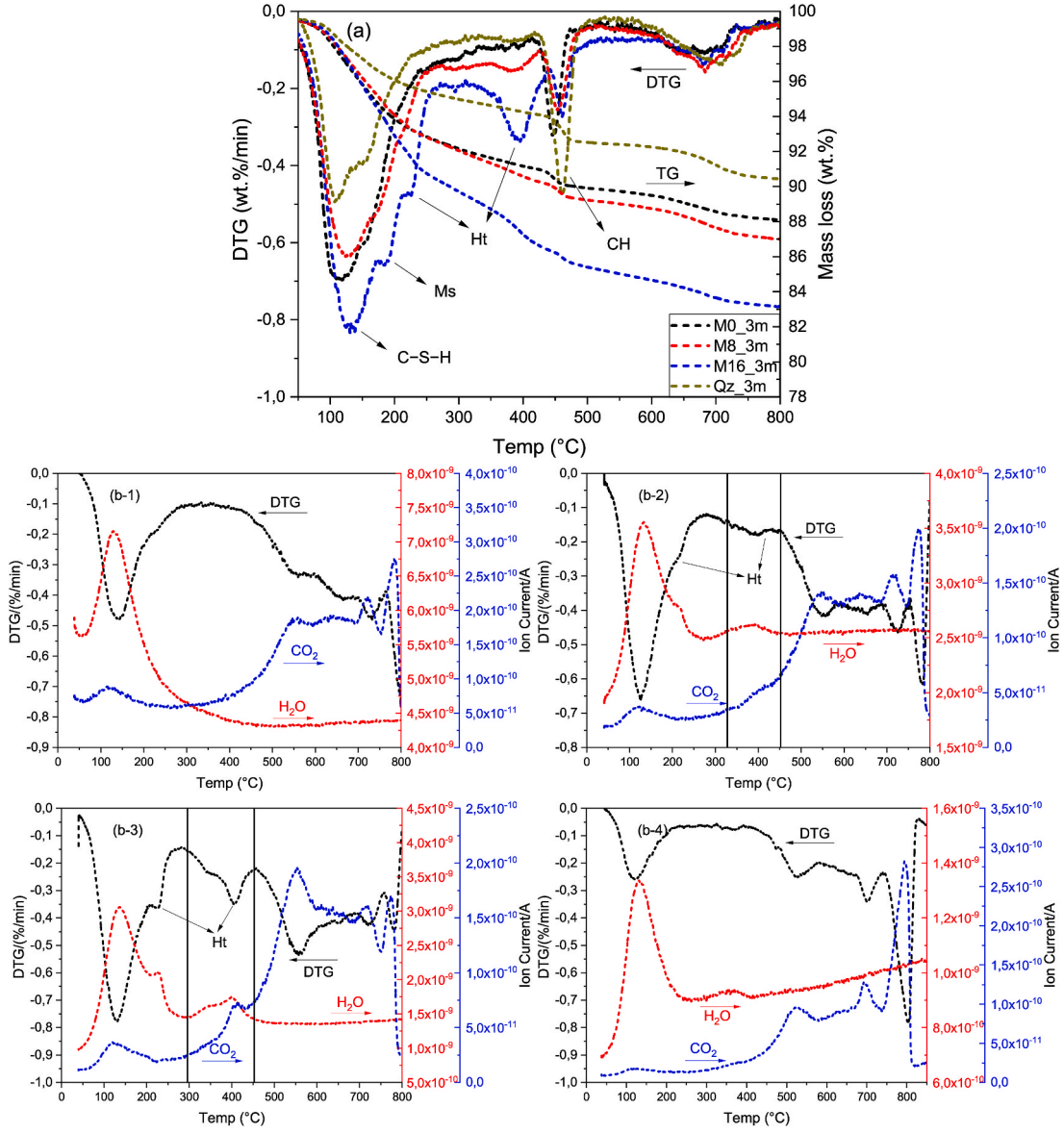

Fig. 4. (a) TG and DTG results of cement-slag and quartz mixtures after 3 months of curing; (b-1)-(b-4) DTG results, H_2O and CO_2 MS curves of fully carbonated cement-slag M0, M8, M16, and Qz pastes, respectively. CH: portlandite; Ms: calcium monosulfoaluminate; Ht: hydrotalcite-like phase.

correspondingly, all of which were commonly seen in the accelerated carbonation test [34–36]. No monosulfate was left, suggesting that it had been carbonated completely. Additionally, there were two new CO_2-bearing phases occurred upon carbonation of cement-slag paste. One was a carbonated hydrotalcite-like phase. The peak located at 350–450 °C indicated the persistence of hydrotalcite-like phase in slag M8 and M16 blends after carbonation. As displayed in the MS curves, both H_2O and CO_2 were liberated from this phase after heating, meaning that CO_2 was absorbed in the interlayer space to replace water molecules and form its carbonate version, i.e., carbonated hydrotalcite-like phase. The small peak at ~150 °C in the MS CO_2 curve should be ascribed to the formation of carbonated Ca–Al AFm phases, due to the carbonation of AFm-SO_4 (monosulfate) and/or AFm-OH phases, which also presented layered microstructure [37,38]. This peak was negligible in cement-Qz mixture, partially because of its reduced monosulfate formation compared to cement-slag pastes.

3.2.2. XRD

XRD results reveal the presence of hydrotalcite-like phase, monosulfate, portlandite, and unhydrated cement clinker (C_3S and C_2S in particular) in cement-slag system after hydration (Fig. 5 (a) and (c)). The peak for hydrotalcite-like phase was much more visible in slag M16 blend, consistent with the results measured by TGA in Fig. 4 (a).

After the accelerated carbonation exposure (Fig. 5 (b) and (c)), the peak for portlandite disappeared in all mixtures, meaning that all calcium hydroxide had been carbonated, in agreement with the results measured by TGA (Fig. 4 (b-1) to (b-3)). Furthermore, the peak for unhydrated cement clinker also vanished, probably related to its continuous hydration or carbonation [39].

Hydrotalcite-like phase was still observed after such a heavy CO_2 attack while monosulfate was decomposed, as the peak of which disappeared after carbonation (Fig. 5 (c)). These results matched well with the findings revealed by TGA. Calcite and Vaterite were identified as the main polymorphs of $CaCO_3$ in all carbonated pastes. No trace of aragonite was found by XRD in these samples. The studies in Ref. [40] pointed out that compared with aragonite, vaterite was formed preferentially on the surface of portlandite due to their similar symmetries and positive surface charge. Also, the environment in the carbonation chamber favored the coexistence of these two polymorphs of $CaCO_3$ [41].

3.2.3. FTIR

FTIR was also used to investigate the carbonation products of cement-slag mixtures, especially the alteration of C–S–H gel phase at molecular level. Fig. 6 illustrates the FTIR spectra of cement-slag mixtures before and after carbonation. The absorption bands between 3700 and 2500 cm^{-1} and at 1640 cm^{-1} indicated the presence of O–H bonds, associated with the stretching and bending vibration modes of H_2O [43]. Because of drying, the intensity of water-related bonds decreased.

Meanwhile, the wave number positions of silicate group in FTIR spectra also implied the presence of different molecular structures of C–S–H gel phase. Depending on the connectivity of silicon site in the $[SiO_4]^{4-}$ tetrahedron (T), the tetrahedron could be classified into five characteristic units based on the representative IR absorption bands, which are; Q^4 (~1200 cm^{-1}), Q^3 (~1100 cm^{-1}), Q^2 (~950 cm^{-1}), Q^1 (~900 cm^{-1}), and Q^0 (~850 cm^{-1}), respectively [44–47]. Regardless of the MgO content in slag, Q^2 was the main unit of C–S–H gel phase of all investigated cement-slag pastes before carbonation. After full carbonation, the Si–O-T stretching band was characterized by observing signals appearing at ~1200 and ~1100 cm^{-1}, which were linked with the yield of Q^4 and Q^3 silicate units, respectively. This shift was associated with the gradual polymerization of silicate units, due to the carbonation-induced decalcification of C–S–H gel phase [48–50].

The carbonate bonds were also recorded through three types of

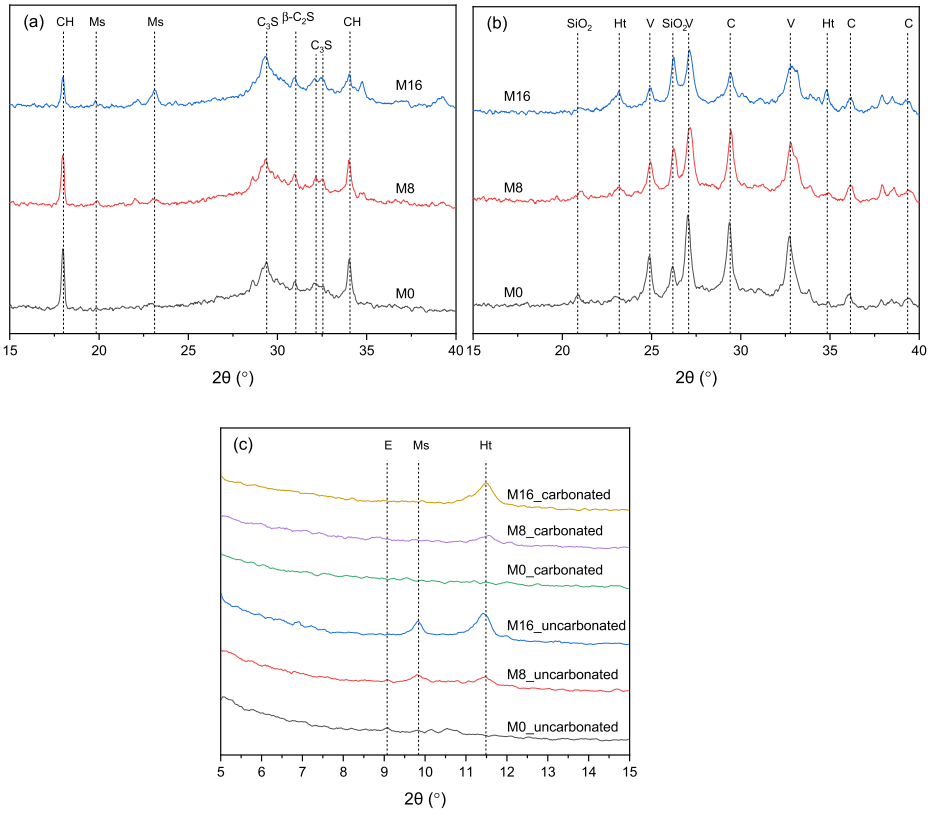

Fig. 5. XRD analysis of cement-slag blends (a) after curing of 3 months; (b) after carbonation; and (c) 5–15° (2θ) of cement-slag blends before and after carbonation. CH: portlandite; E: ettringite; Ht: hydrotalcite-like phase. V: vaterite; C: calcite. The peak centered at around 2θ = 21 and 26° appeared to be associated with the formation of silica gel (labelled as SiO_2) due to the carbonation of C–S–H gel phase [42].

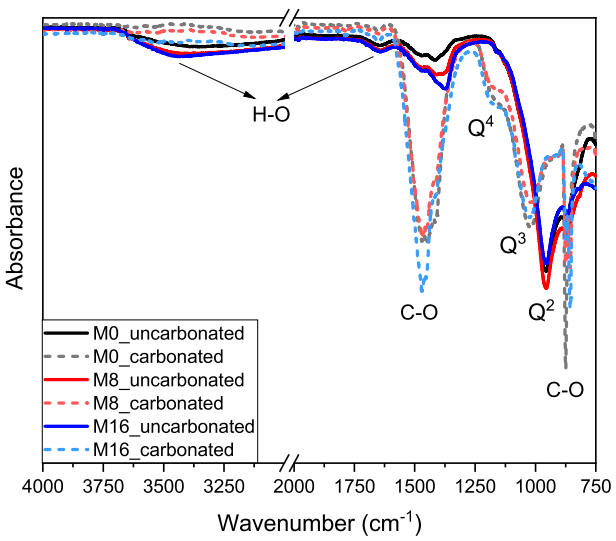

Fig. 6. The FTIR spectra of cement-slag mixtures before and after carbonation.

carbonate bands observed in the FTIR spectra, i.e., strong broad band at 1400-1500 cm^{-1}, representing the asymmetric stretching of carbonate, narrow band at 875-1000 cm^{-1} due to the bending of carbonate, and in-plane bending of carbonate at ~710 cm^{-1} (not shown in the graph) [40]. It was found that the CO_2 bound was more pronounced in cement-slag M16 paste, confirmed by the increased band intensity at 1400-1500 cm^{-1}.

3.3. Degree of CO_2 uptake of different carbonate phases

To calculate the CO_2 concentration in each carbonate phase at different depths, besides that taken from 0–3 mm depth from the surface corresponding to full carbonation (labelled as 1), powders were also extracted from carbonation front corresponding roughly to transitional/dissolution area (labelled as 2) [51], and mildly/non-carbonated area (labelled as 3), respectively as Fig. 7 shows.

As mentioned earlier, pure $CaCO_3$ was employed as a standard to calibrate the CO_2 concentration in different CO_2-bearing phases under the same analytical condition. Fig. 8 (a) shows the DTG result, CO_2 MS curve of pure $CaCO_3$. The area under the MS CO_2 curve (A•°C) corresponding to 44 wt% CO_2 releasing from $CaCO_3$ was calculated using commercial software OriginPro 2019. Comparatively, the CO_2 concentration of each carbonate phase can thus be estimated from the area under the CO_2 MS curve within the corresponding temperature range as shown in Fig. 8(b–d) which presented the CO2 uptake profile of slag M16 paste at the specific sampling depths. The area A1, A2, and A3 corresponded to the amount of CO_2 released from carbonated Ca–Al AFm phases, carbonated hydrotalcite-like phase, and calcium carbonate, respectively.

It was well recognized that various forms of $CaCO_3$, including amorphous $CaCO_3$, metastable $CaCO_3$ (aragonite and vaterite), and calcite were present simultaneously in a carbonated cement-based

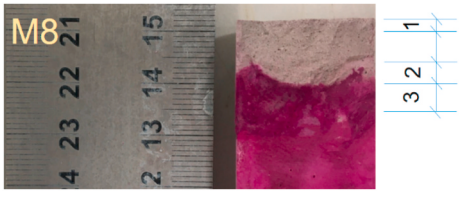

Fig. 7. The positions where powders were extracted, using slag M8 paste as an example. 1: fully carbonated area; 2: transitional area; 3: mildly carbonated area.

system [34–36]. However, the coexistence of these forms of $CaCO_3$ had no effect on the determination of CO_2 amount bound in $CaCO_3$ through thermogravimetric analysis, and thus it was unnecessary to separate them rigorously.

The calculated areas under the MS CO_2 curves and the CO_2 concentrations of the paste samples and the calibration reagent are shown in Tables 3 and 4, respectively. It was noticed that carbonated Ca–Al AFm phases played a minor role in absorbing CO_2, while the CO_2 binding capacity of each mixture was mainly dependent on the available CaO in portlandite and C–S–H gel phase. The role of hydrotalcite-like phase in absorbing CO_2 started to emerge with the gradual addition of MgO in slag, and its binding ability was positively related to its content after hydration. It should be noted that the most hydrotalcite-like phase was detected in slag M16 paste (Fig. 4 (a) and Fig. 5 (a)), where it was able to absorb up to ~2.68 g/100 g paste CO_2 in the interlayer space.

Moreover, it was interesting to find that the highest amount of CO_2 was bound in slag M16 paste in the fully carbonated area. On the other hand, the same paste absorbed the least amount of CO_2 in the mildly carbonated and transitional areas, compared to the other mixtures.

3.4. Microstructure

In this section and section 3.5, the authors attempted to analyze the impact of carbonation on microstructure development, elemental composition of the phase assemblages, and micro-mechanical evolution. Samples used for measurements were selected from the carbonated area (colorless appearance after phenolphthalein spray) for each mixture.

3.4.1. MIP

Relative to the cement-quartz system, hydrates formed from the reaction between portlandite and slag helped refine the pore structure, which is shown clearly in Fig. 9 (a) and (c).

Generally, the critical pore diameter of cement-slag blends was less than 0.01 μm, corresponding to medium capillary pores based on the classification put forward in Ref. [52]. The value decreased significantly with increasing MgO content in slag. Moreover, it was noted that cement-slag M0 and quartz mixtures presented a bimodal pore structure while slag M8 and M16 pastes appeared to be a unimodal one. One should keep in mind that the maximum pressure that the equipment can apply was 210 MPa, and thus pore diameter smaller than ~7 nm (gel pore) cannot be detected here. Therefore, it was foreseeable that the critical pore diameter of cement-slag M16 blend would be smaller than 7 nm according to the trend of curve shown in Fig. 9 (a).

After accelerated carbonation test, the critical pore diameter all shifted right to the range of 0.1–100 μm, depending on the amount of magnesia in slag. It indicated a coarser pore structure was created after carbonation, due to the carbonation of overwhelming amount of C–S–H gel phase. Similar results were also reported in Refs. [42,53–55]. The carbonation of C–S–H gel phase would produce a poorly organized silica gel of a low molar volume and a certain amount of free water initially bound within the gel phase, which certainly led to an increase in porosity.

Besides, pores in the range of 10–100 μm appeared in slag M0 and M8 pastes after carbonation. It was possibly ascribed to the formation of micro-cracks owing to carbonation shrinkage. Especially for the carbonation of low Ca/Si ratio C–S–H gel phase originated from the pozzolanic reaction, it can produce relatively large shrinkage [56], leading to a higher potential for the formation of micro-cracks. It was also reflected by the cumulative intrusion curve shown in Fig. 9 (d). The more magnesia in slag, the lower porosity after carbonation. As confirmed in Tables 3 and 4, the rich production of hydrotalcite-like phase in slag M16 mixture shared more CO_2 in the mildly carbonated and transitional areas. Also, the additional hydration of slag (Fig. 12 (b)) further help in densification of microstructure, leading to a reduced porosity.

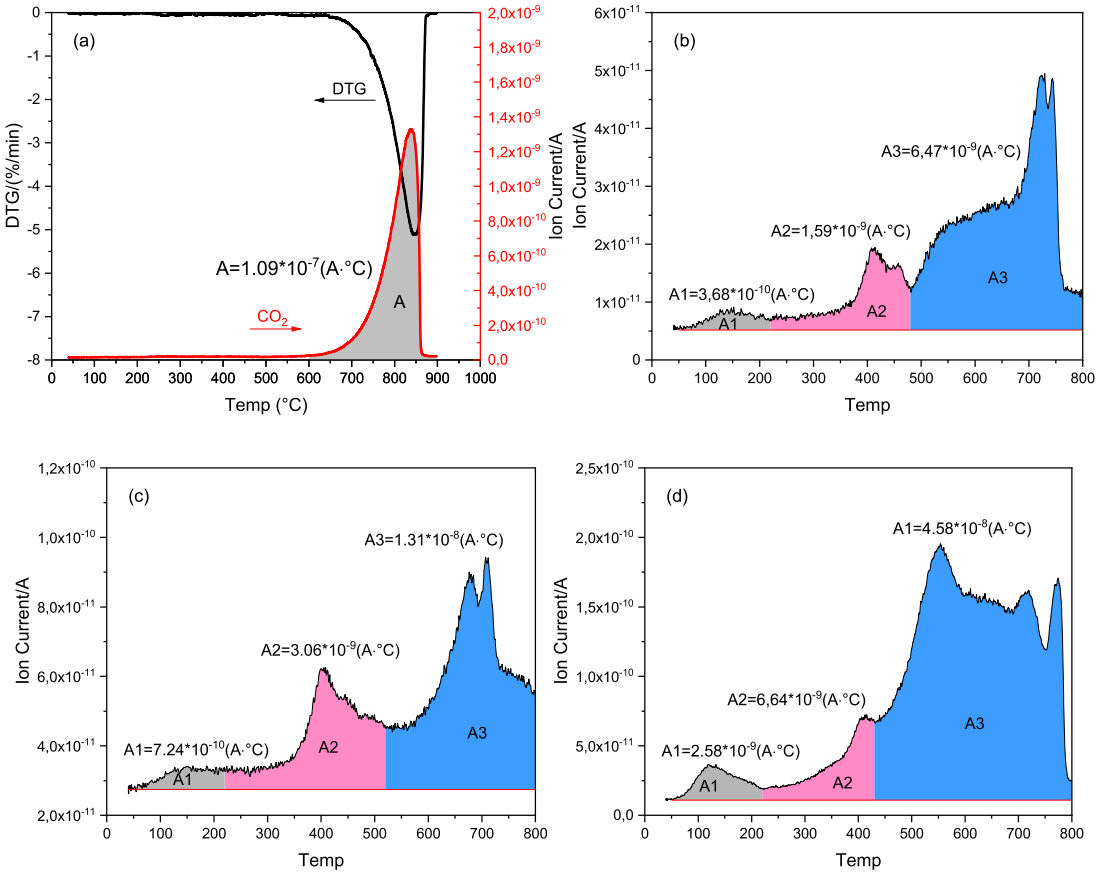

Fig. 8. (a) The DTG result, CO_2 MS curve of pure $CaCO_3$; (b–d) The CO_2 MS curve of slag M16 paste at mildly carbonated, transitional, and fully carbonated areas, respectively.

Table 3
The calculated area under the MS CO_2 curve of different carbonate phases (A•°C).

		Area under the MS CO_2 curve			Total
		Carbonated Ca–Al AFm phases	Carbonated hydrotalcite-like phase	Calcium carbonate	
Mildly carbonated	M0	4.79×10^{-10}	–	9.37×10^{-9}	9.85×10^{-9}
	M8	3.23×10^{-10}	1.18×10^{-9}	7.67×10^{-9}	9.17×10^{-9}
	M16	3.68×10^{-10}	1.59×10^{-9}	6.47×10^{-9}	8.43×10^{-9}
Transitional	M0	6.55×10^{-10}	–	2.59×10^{-8}	2.65×10^{-8}
	M8	4.58×10^{-10}	2.92×10^{-9}	1.79×10^{-8}	2.12×10^{-8}
	M16	7.24×10^{-10}	3.06×10^{-9}	1.31×10^{-8}	1.69×10^{-8}
Fully carbonated	M0	2.91×10^{-9}	–	3.92×10^{-8}	4.21×10^{-8}
	M16	2.58×10^{-9}	6.64×10^{-9}	4.58×10^{-8}	5.50×10^{-8}
	Qz	1.50×10^{-9}	–	3.81×10^{-8}	3.96×10^{-8}
	Pure $CaCO_3$	–	–	1.09×10^{-7}	1.09×10^{-7}

Table 4
CO_2 concentration of different carbonate phases based on the pure $CaCO_3$ (/100 g) calibration.

		CO_2 concentration of each carbonate phase			Total
		Carbonated Ca–Al AFm phases	Carbonated hydrotalcite-like phase	Calcium carbonate	
Mildly carbonated	M0	0.19	–	3.79	3.98
	M8	0.13	0.48	3.09	3.70
	M16	0.15	0.64	2.61	3.40
Transitional	M0	0.25	–	10.45	10.70
	M8	0.17	1.17	7.22	8.56
	M16	0.30	1.23	5.29	6.82
Fully carbonated	M0	1.17	–	15.82	16.99
	M8	0.85	1.61	16.11	18.57
	M16	1.03	2.68	18.49	22.20
	Qz	0.51	–	15.38	15.99
	Pure $CaCO_3$	–	–	44.0	44.0

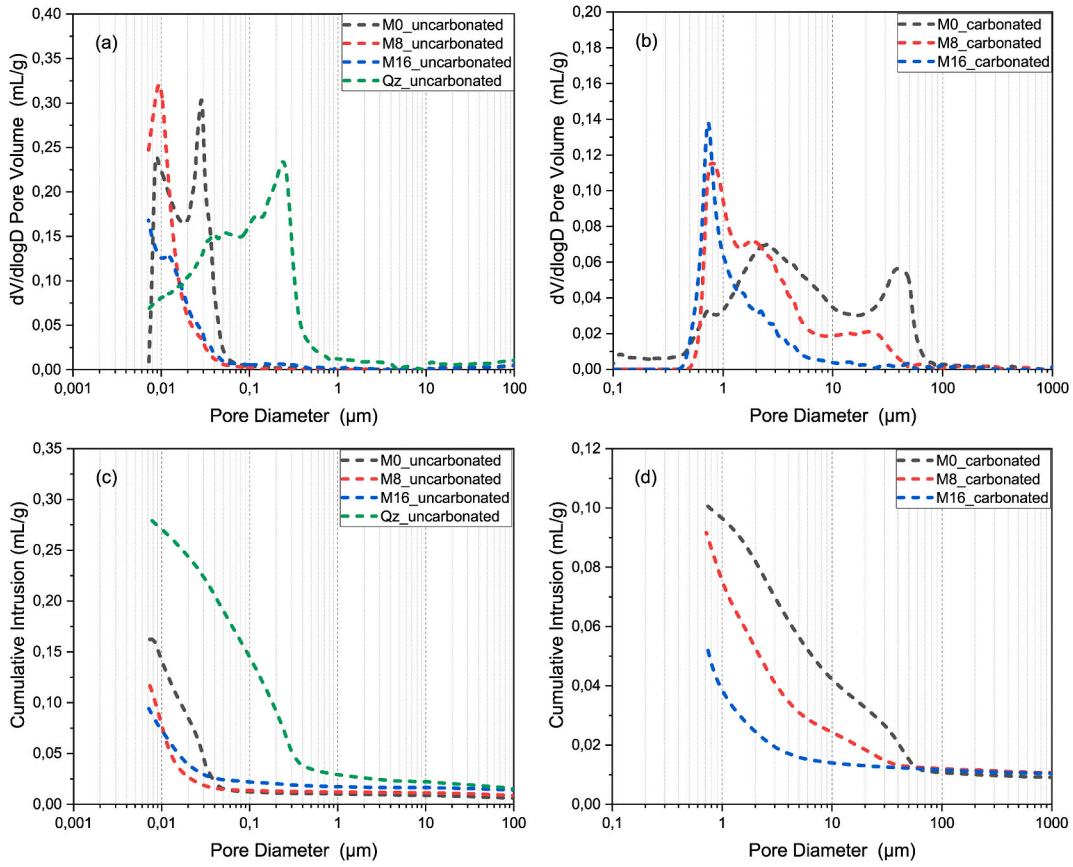

Fig. 9. Differential pore size distribution of cement-slag and quartz systems measured (a) before and (b) after accelerated carbonation test; Cumulative intrusion of cement-slag and quartz systems measured (c) before and (d) after accelerated carbonation test.

3.4.2. SEM-BSE

Fig. 10 illustrates the typical microstructure of cement-slag paste before and after accelerated carbonation testing (in the carbonated area). A small amount of unhydrated cement grains (circled and labelled as #1 in Fig. 10 (a-1)) were distributed in the matrix together with mass of unhydrated slag particles after 3 months of curing. Calcium monosulfoaluminate existed as fine and compact crystals intermixed with C–S–H gel phase (circled and labelled as #2 in Fig. 10 (a-1)). Slag hydrated slowly, and the hydrates precipitated at the rim of the unreacted slag particle (especially for slag M16 paste in Fig. 10 (c-1)), forming a dense transition into the surrounding matrix. Visually, the matrices of slag M8 and M16 pastes were more homogeneous and denser than that of slag M0.

The difference manifested in the microstructure of matrix among these slag cement pastes was even more evident after accelerated carbonation testing (Fig. 10 (a-2) to (c-2)). Overall, they appeared more porous with a large quantity of black spots, indicating the formation of pores filled with epoxy resin. Moreover, slag M0 paste had developed network of wide cracks as shown in Fig. 10 (a-2) (To display the morphology of crack, the magnification of this BSE image was set at 1000 × .). It verified the critical pore diameter in the range of 10–100 μm appearing in slag M0 paste after carbonation by MIP test. The most striking result was observed from the microstructure of carbonated slag M16 paste as shown in Fig. 10 (c-2), as most of the microstructure was not affected by the carbonation process. Unreacted slag grains hydrated continuously under CO_2 attack, and the rim of slag after accelerated carbonation testing was significantly thicker than before the carbonation. According to the results in Ref. [57], a demand for calcium ions was created in the pore solution during carbonation, leading to the migration of highly mobile calcium ions forming from the dissolution of unhydrated slag grains outwards, thus promoting the formation of thicker rims. One should keep in mind that the continuous hydration of slag was concluded from the thicker slag rim by observation roughly. To further verify this idea, determining the hydration degree of slag through e.g., BSE image analysis before and after carbonation was recommended.

3.4.3. Chemical composition

3.4.3.1. C–S–H gel phase. The elemental composition of cement matrix and rim around unhydrated slag grain were characterized before and after carbonation by SEM-EDS microanalysis with internal standards (standardless microanalysis). Typical plots of Al/Ca against Si/Ca in atomic ratios are presented in Fig. 11. In general, the measured Ca/Si atomic ratios of C–S–H gel phase after 3 months of curing fluctuated at around 1.20, irrespective of the amount of MgO incorporated into slag. It was in good agreement with the values determined in Refs. [58–60]. However, substantial decalcification occurred in the blended systems, and two different types of C–S–H gel phase existed in the matrix after the accelerated carbonation exposure [61,62]. Especially for slag M0 paste (Fig. 11 (a)), the Ca/Si ratio reduced more significantly compared with that of slag M16 paste (Fig. 11 (b)). Besides, it was also found that the Al/Si atomic ratio of the decalcified C–S–H gel phase was considerably higher than that of unaffected gel phase, further confirming the occurrence of amorphous alumina gel along with carbonation [62].

3.4.3.2. Hydrotalcite-like phase. As for hydrotalcite-like phase, it seemed to be unaffected by CO_2 attack. The Mg/Al atomic ratio derived from the regression analysis of Mg/Si vs. Al/Si scatter plot (Fig. 12) remained nearly the same before and after carbonation. It also indicated that this phase kept intact during carbonation. In other words, the CO_2 uptake in the interlayer space would not decompose the network

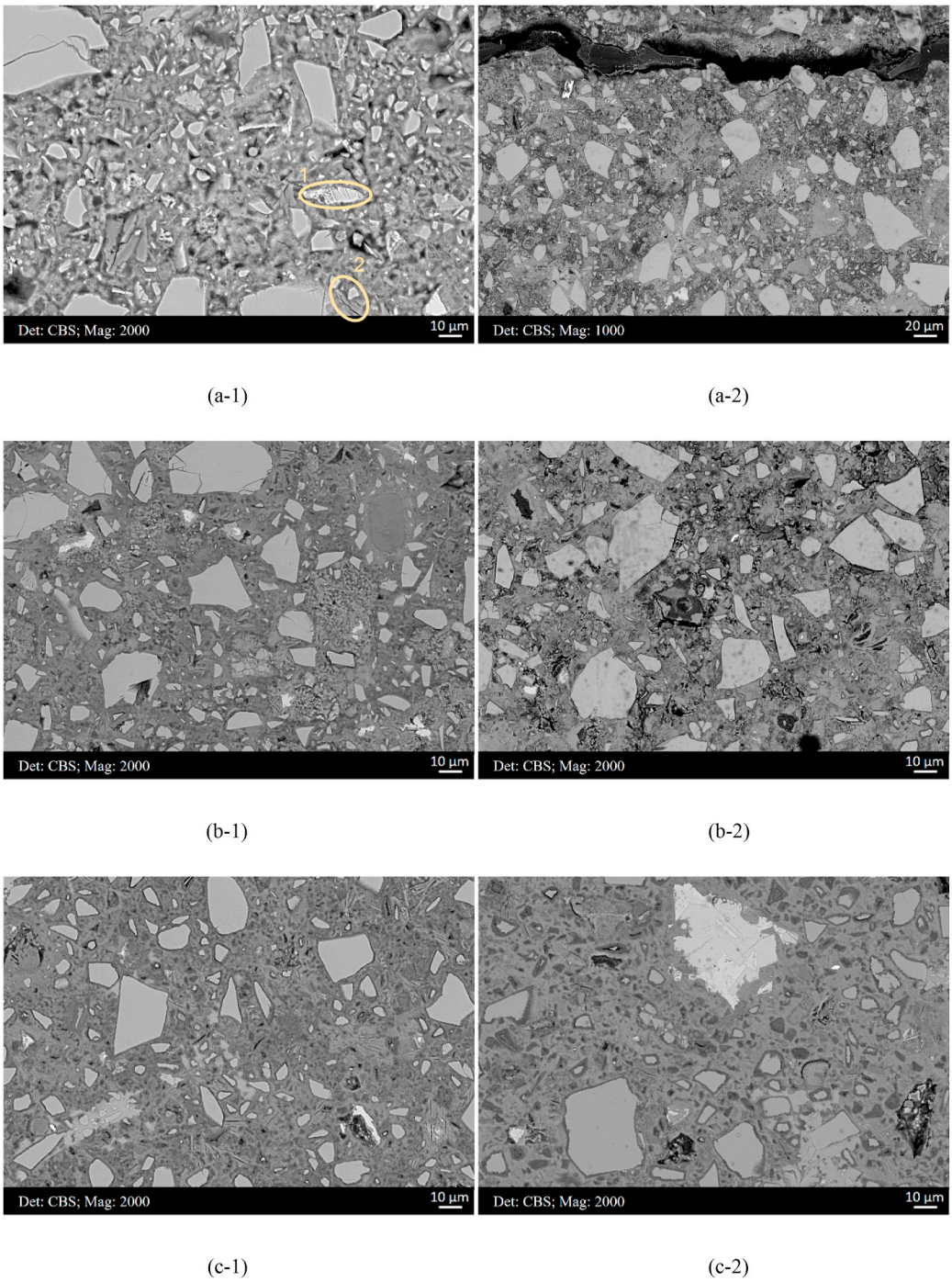

Figs. 10. (a-1) to (c-1): Microstructure of cement-slag M0, M8, and M16 mixtures after 3 months of curing, respectively; and (a-2) to (c-2): Carbonated area of cement-slag M0, M8, and M16 mixtures after carbonation, respectively.

structure of hydrotalcite-like phase. The occurrence of scatter points with significantly higher Mg/Si and Al/Si values (circled in Fig. 12 (b)) demonstrated that slag grains in the carbonated area of M16 paste hydrated continuously during carbonation, consistent with the thicker rims illustrated by BSE image shown in Fig. 10 (c-2).

3.5. Micro-mechanical properties

To obtain the micro-mechanical properties of the cement matrices, especially C–S–H gel phase before and after the accelerated carbonation testing, around 800 nanoindentations were made for each mixture. For the detailed statistical deconvolution process of the nanoindentation results, please refer to Ref. [63].

The relative frequency of indentation modulus obtained from the samples after 3 months of curing are shown in Fig. 13 (a-1) to (c-1). The highest peak in the frequency histogram was quite narrow with a low variance, which was supposed to be C–S–H gel phase. It was determined as 17.74 ± 5.27 GPa for this phase in slag M0 blend. On the other hand, two C–S–H gel phases were separated in the other two blends, i.e., 17.66 ± 2.99 GPa together with 20.83 ± 7.63 GPa in slag M8 mixture, and 21.28 ± 2.17 GPa as well as 23.72 ± 7.10 GPa in slag M16 mixture, corresponding to low density and high density C–S–H gel phase, respectively. Meanwhile, it was noted that the peak regarding high density C–S–H gel phase was a little broader, probably overlapped with

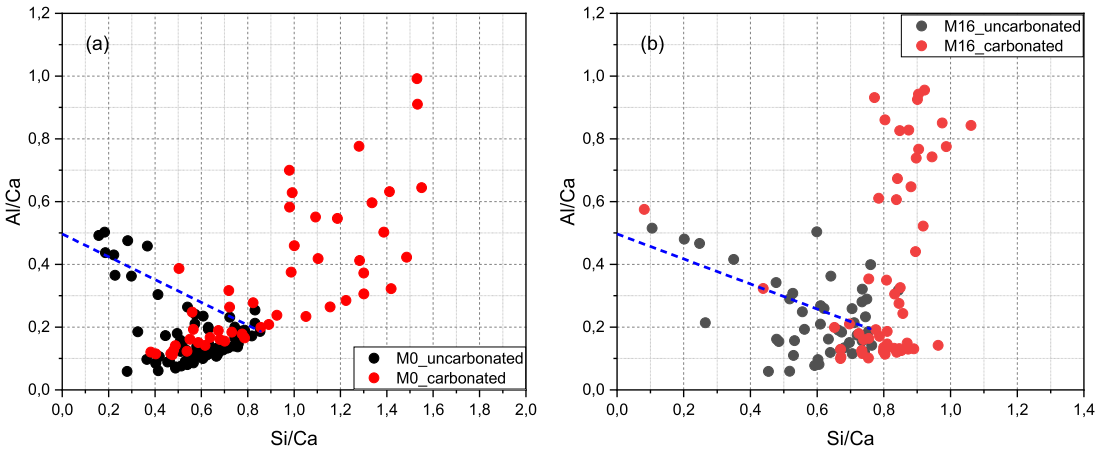

Fig. 11. Typical plots of Al/Ca against Si/Ca in atomic ratio of slag (a) M0 and (b) M16 pastes before and after carbonation.

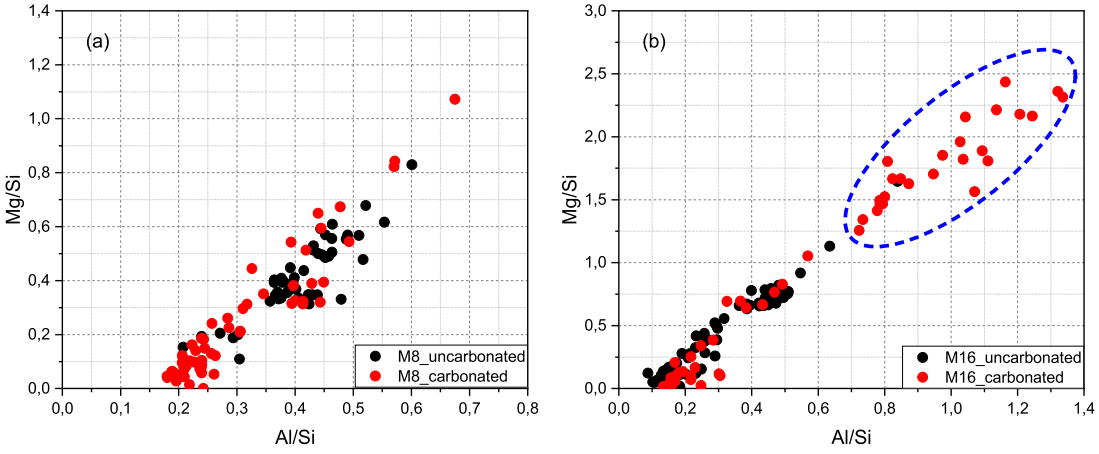

Fig. 12. Typical plots of Mg/Si against Al/Si in atomic ratio of slag (a) M8 and (b) M16 pastes before and after carbonation.

neighboring phases, including low density C–S–H gel phase [64–66] and calcium hydroxide [67]. Moreover, the Gaussian peak below 4 GPa in slag M0 system was believed to be linked to the pores in the testing area. This peak vanished in the other two blends, implying a denser and less porous matrix was obtained. This result agreed well with the MIP measurement reported in Fig. 9 (a) and BSE micrographs illustrated in Fig. 10 (a-1) to (c-1), where with the increasing MgO content of slag, the porosity of cement-slag system decreased.

The hump centered at 31.09 ± 8.95 GPa in slag M0 blend was associated with the wide presence of portlandite due to its relatively low reactivity [16]. This small peak shifted right to 44.18 ± 14.27 GPa and 39.06 ± 14.02 GPa in slag M8 and M16 mixtures, respectively. This can be explained in two ways: (1) more portlandite was consumed by pozzolanic reaction in these two mixtures and thus more hydrotalcite-like phase was precipitated. The work in Ref. [68] found that the indentation modulus of hydrotalcite-like phase was larger than 40 GPa roughly. (2) values from unreacted slag grains (>50 GPa commonly) were also incorporated in this broad peak.

Compared with the uncarbonated samples, the major difference occurring in the carbonated pastes was the reduction of modulus value of C–S–H gel phase, due to its degradation or decalcification after CO_2 attack (Fig. 13 (a-2) to (c-2)). In slag M0 and M8 blends, the frequency distribution of C–S–H gel phase indentation modulus was found to exhibit a bimodal distribution, centered at 8.71 ± 3.34 GPa together with 18.07 ± 5.18 GPa for slag M0 mixture, and 11.44 ± 2.78 GPa as well as 20.08 ± 3.40 GPa for slag M8 mixture, corresponding to the degraded and unaffected C–S–H gel phase, respectively. Furthermore, the frequency density of degraded C–S–H gel phase even exceeded that of unaffected in slag M0 paste after carbonation.

However, in slag M16 mixture, there was no obvious decrease observed for the indentation modulus of C–S–H gel phase in the carbonated area. The corresponding values before and after carbonation were nearly the same. The result agreed with the BSE micrographs shown in Fig. 10 (c-2), where large areas were unaffected by carbonation.

Here in the carbonated pastes, the peak centered at around 30 GPa should include the contribution from carbonates [69,70]. These carbonates, existing in different forms, had been found to accumulate in the pores and interact with C–S–H gel phase as well as portlandite by a strong ionic-covalent bond [71].

4. Discussion

4.1. Distribution of Mg after carbonation

It is well known that owing to its low diffusion ability, magnesium dissolved from slag cannot move into cement matrix during hydration. Fig. 14 reveals a typical BSE micrograph of carbonated slag M8 paste, and the Mg and Al mappings correspondingly. Compared with aluminum, magnesium still appeared to be distributed within the original slag grain region, and cannot diffuse into the matrix although C–S–H gel phase surrounding slag particles was degraded remarkably. The matrix became porous after carbonation, e.g., the top left and bottom right regions of the micrograph. In other words, hydrotalcite-like phase

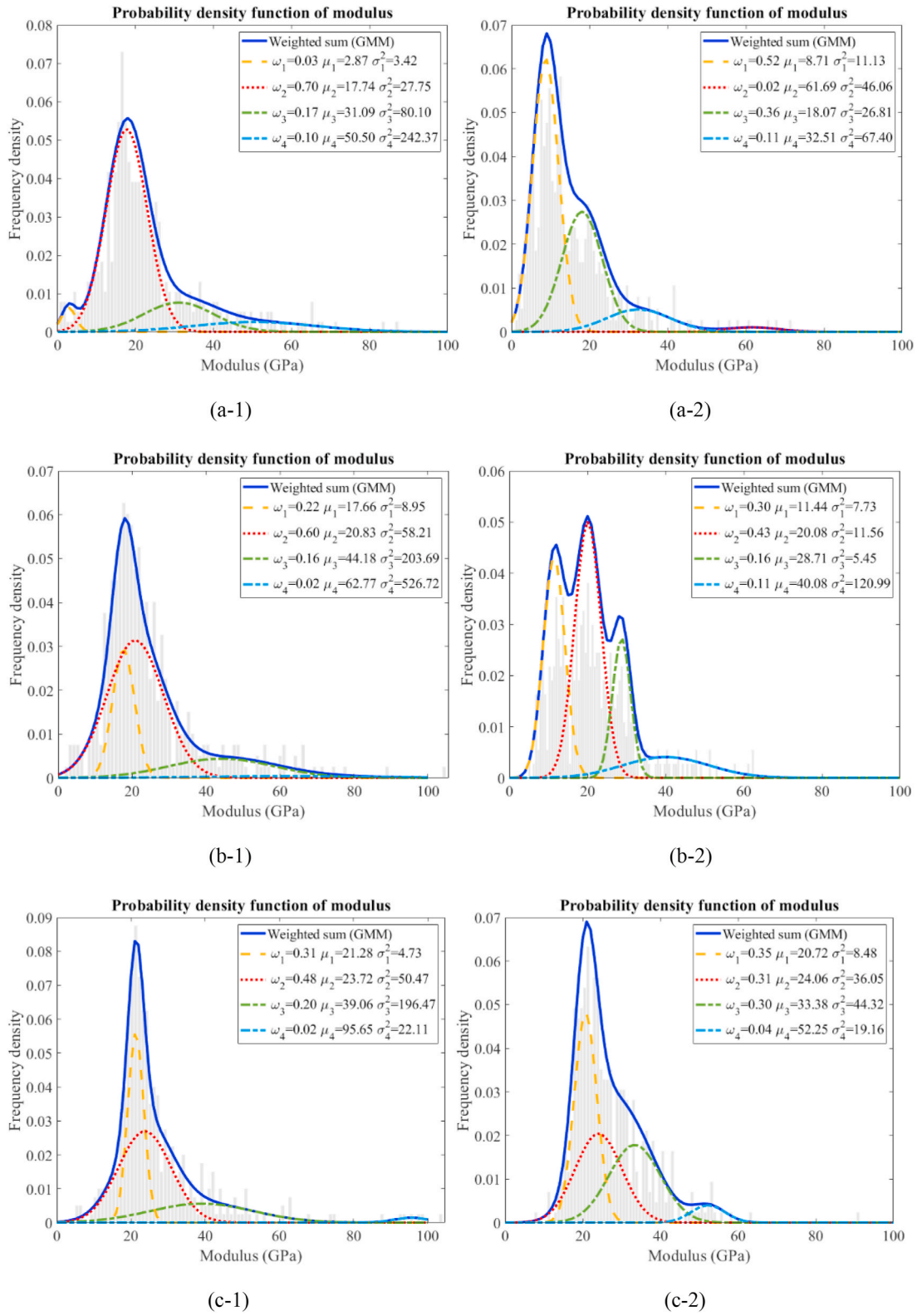

Fig. 13. Indentation modulus of (a-1) to (c-1): cement-slag M0, M8, and M16 mixtures after 3 months of curing, respectively; and (a-2) to (c-2): the carbonated area of cement-slag M0, M8, and M16 mixtures, respectively.

formed in slag rim was able to remain intact during carbonation. It further confirmed the results found in TGA (Fig. 5 (b-2) and (b-3)) and XRD (Fig. 6 (c)), both of which identified its persistence even in the fully carbonated area. In addition, the Mg/Al atomic ratio derived from the regression analysis of Mg/Si vs. Al/Si scatter plot (Fig. 12) also remained nearly the same before and after carbonation. These findings were consistent with the results from Ref. [50], which also concluded that the hydrotalcite-like phase seemed to be stable towards carbonation.

It was commonly recognized that the carbonation rate of cement blended with slag was generally higher than that of pure cement due to

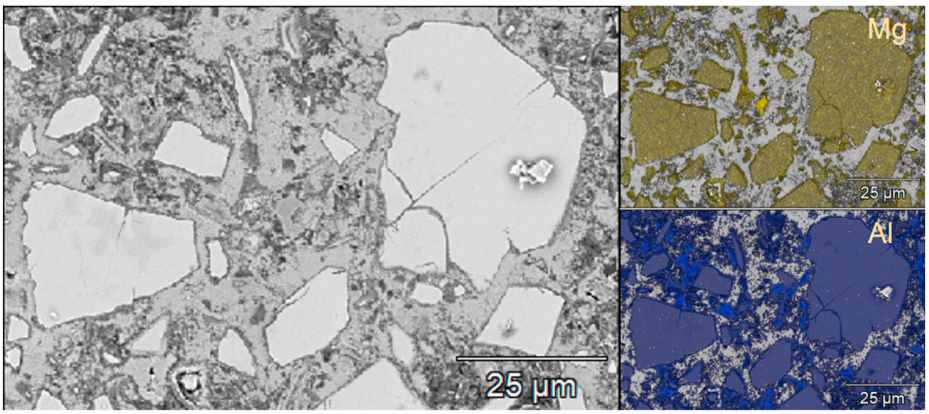

Fig. 14. Left: a typical BSE micrograph of carbonated slag M8 paste, and right top and bottom: the Mg and Al mappings correspondingly.

its lower calcium hydroxide and higher C–S–H gel phase content [42, 72–75]. The carbonation between portlandite and CO_2 was a volume expansion reaction, and the main reaction product, i.e., different forms of calcium carbonate could help refine the pore structure, preventing the further ingress of CO_2. However, the carbonation of C–S–H gel phase was a volume shrinkage process, coarsening the pore structure and increasing the porosity [42,55,61,76]. Different from reactions mentioned above, hydrotalcite-like phase binds CO_2 in the interlayer space and maintains its network structure during carbonation, thus few volumetric changes are observed during this process [77]. From this point of view, increasing the amount of hydrotalcite-like phase produced in the system, or increasing MgO content of slag, was definitely beneficial for improving the carbonation resistance of cement-slag system.

4.2. CO_2 binding of hydrotalcite-like phase at different depths

Generally, the carbonation resistance of cement-based systems is dependent on two factors: the alkali content (phase composition and particularly portlandite content) and the pore structure. Portlandite and C–S–H gel phase are considered as the main CO_2 binding phases in the blended cement [61]. However, the role of hydrotalcite-like phase in absorbing CO_2 has been neglected, especially when the substitution level of slag is high, e.g., as in CEM III/B.

As shown in Tables 3 and 4, when shifting from mildly carbonated area to fully carbonated area, the absolute amount of CO_2 absorbed in each carbonate phase increases correspondingly. However, the proportion distributed among them was the opposite. The proportion of CO_2 absorbed into carbonated Ca–Al AFm phases was minor, fluctuating at less than 5%. The proportion in carbonated hydrotalcite-like phase went down while the calcium carbonate share went up. It was clearly illustrated by the ratio of CO_2 amount absorbed by carbonated hydrotalcite-like phase to calcium carbonate (Fig. 15). Regardless of the MgO content of slag, this ratio decreased significantly when entering into the totally carbonated area.

It illustrates us a different routine about the carbonation sequence of hydration products in cement-slag system. Initially, hydrotalcite-like phase, portlandite, and C–S–H gel phase absorb CO_2 synchronously. Especially for hydrotalcite-like phase, due to its stacked layer morphology, the space between layers presents a specific surface area comparable to that of C–S–H gel phase [78], and provide the natural site to fix free CO_2 molecules [79,80]. It shares more than 15% CO_2 in the mildly carbonated and transitional areas, and this value is positively associated with the magnesia content of slag. Probably due to the complete carbonation of hydrotalcite-like phase, the proportion of CO_2 bound by hydrotalcite-like phase decreases in the fully carbonated area, and more CO_2 is fixed into calcium carbonate at this depth.

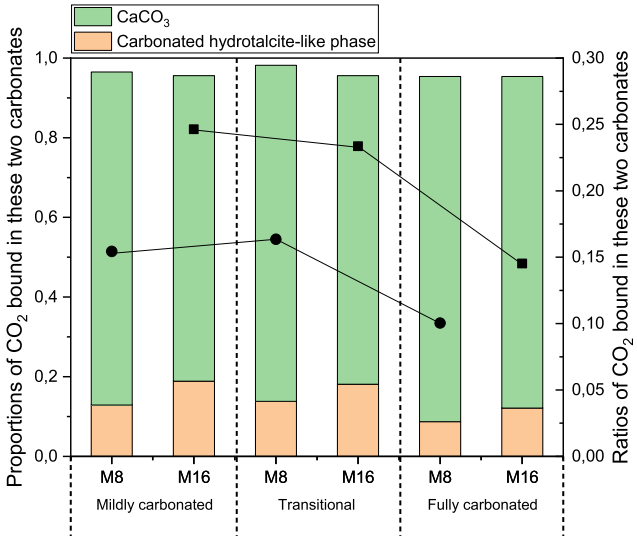

Fig. 15. The proportion of CO_2 bound in $CaCO_3$ and carbonated hydrotalcite-like phase, and the ratio between these two phases from mildly to fully carbonated area.

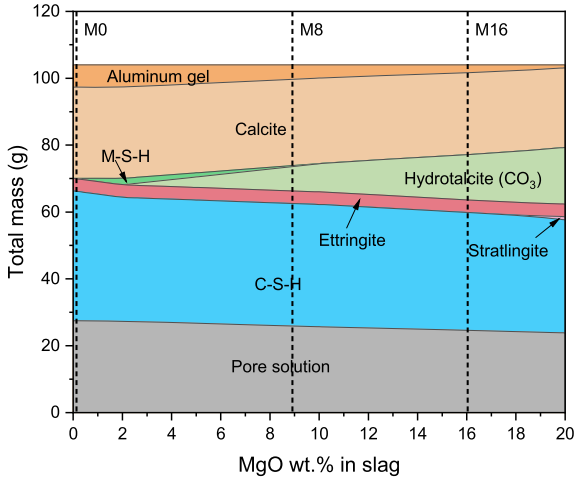

Fig. 16. Thermodynamic modelling of the phase assemblages of cement-slag system with the gradual addition of MgO at a certain amount of CO_2 uptake (10 g CO_2/100 g binder).

4.3. Thermodynamic modelling

Fig. 16 presents the evolution of phase assemblages at 10 g CO_2/100 g binder as a function of MgO content of slag. The reaction degree of clinker phases of cement at 90 days was estimated using the empirical kinetic approach proposed by Parrot and Killoh [81], and it was assumed that 30% slag dissolved during the period. For simplicity, it was postulated that each component of slag dissolved congruently.

The main CO_2-binding phase in slag M0 mixture was $CaCO_3$, while more CO_2 was absorbed in hydrotalcite-like phase and less in $CaCO_3$ as a result in slag M16 mixture. In the initial stage, hydrotalcite-like phase was unaffected by CO_2 attack, then it transformed into the carbonate form, namely hydrotalcite-like phase (CO_3) in the graph. This phase was able to keep intact for a continuous CO_2 supply and converted to magnesium silicate hydrate (M−S–H) gel in the later stage, and dolomite ($MgCa(CO_3)_2$) was assumed to be the final Mg-bearing phase. However, based on the experimental results in the present research, hydrotalcite-like phase would absorb CO_2 upon carbonation. Meanwhile, carbonated hydrotalcite-like phase was not observed to decompose in this paper. These disagreements identified between experimental and modelling results need more research in the future.

When concentrating on carbonated hydrotalcite-like phase and calcium carbonate, thermodynamic modelling also illustrates a decreasing trend regarding the ratio of CO_2 amount bound in these two phases (C_{Ht}/C_{cc}) (Fig. 17). This trend was consistent with the experimental results shown in Fig. 15. Roughly, we can also divide the graph into three zones where the progress of CO_2 uptake in slag cement systems can be explained. According to the experimental and modelling findings, initially, hydrotalcite-like phase starts to absorb the carbonate ions earlier due to the low solubility product of its carbonate forms [32,77], thus, a relatively high (C_{Ht}/C_{cc}) ratio is observed in the mildly carbonated area. With the continuous supply of CO_2, the (C_{Ht}/C_{cc}) ratio decreases in the transitional area as the CO_2-binding ability of these two phases are remarkably different (44/100 (wt/wt) for $CaCO_3$ and 44/484 (wt/wt) for $Mg_4Al_2(OH)_{12}(CO_3)\bullet 4(H_2O)$), and more CO_2 was fixed into $CaCO_3$. Finally in the fully carbonated zone, hydrotalcite-like phase cannot absorb CO_2 anymore, which facilitates formation of $CaCO_3$ upon new CO_2 ingress, decreasing the (CHt/Ccc) ratio further.

5. Conclusions

In this research we investigated the effect of MgO content of slag on the carbonation characteristics of specific cement-slag systems through accelerated carbonation testing and focused on the quantitative role of hydrotalcite-like phase, in particular. The main conclusions drawn were as follows:

- The gradual increase of MgO in slag composition did not change the mineralogy of carbonation products fundamentally. While calcium carbonate was the main CO_2-bearing phase, hydrotalcite-like phase and Ca–Al AFm phases did absorb almost 20 wt% of the entire bound CO_2, as well. Calcite and vaterite were identified as the main polymorphs of $CaCO_3$ in all pastes.
- After the accelerated carbonation testing, the critical pore diameter in slag cement paste increased to the range of 0.1–100 μm, depending on the amount of magnesia in slag. The critical pore diameter in the range of 10–100 μm appeared in slag M0 and M8 pastes after carbonation was possibly ascribed to the formation of micro-cracks caused by carbonation shrinkage.
- There were large areas unaffected by the carbonation process in slag M16 paste in the carbonated zone, and unreacted slag grains hydrated continuously during carbonation. As it was also reflected by nanoindentation testing, there was no obvious decrease observed on the indentation modulus of C–S–H gel phase in slag M16 paste, while it reduced significantly for slag M0 and M8 pastes.

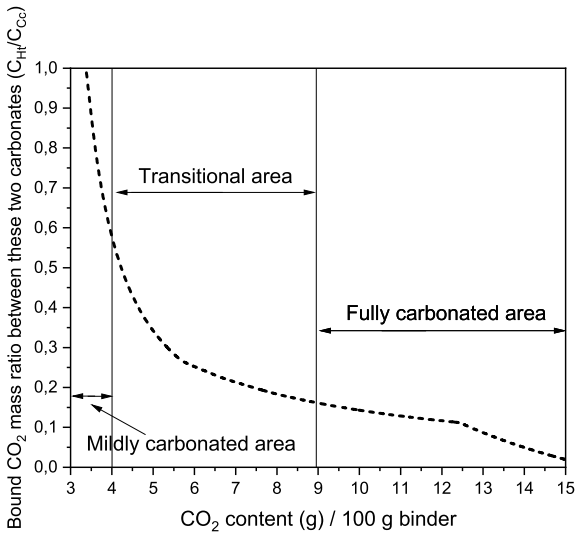

Fig. 17. The ratio of CO_2 bound in carbonated hydrotalcite-like phase to $CaCO_3$ with the gradual ingress of CO_2 through modelling.

- Hydrotalcite-like phase can maintain its network structure and remain intact during carbonation (i.e., binding CO_2 in its interlayer space). Thus, magnesium was still contained within the original slag grain region, and the Mg/Al atomic ratio remained nearly the same before and after carbonation.
- Hydrotalcite-like phase shared more than 15% CO_2 in the mildly carbonated and transitional zones, and this value was positively correlated with the magnesia content of slag. The proportion decreased in the fully carbonated area, and more CO_2 was fixed into calcium carbonate. It was consistent with the thermodynamic modelling that the ratio of CO_2 bound in carbonated hydrotalcite-like phase to $CaCO_3$ decreased continuously with the gradual ingress of CO_2.

Declaration of competing interest

The authors declare that they have no known competing financial interests or personal relationships that could have appeared to influence the work reported in this paper.

Data availability

Data will be made available on request.

Acknowledgements

The authors are grateful for the China Scholarship Council (Grant Number 201808320456 and 202007000027) and BAM Infraconsult B.V. for their financial support. Authors also thank Arjan Thijssen (Microlab, Delft University of Technology) for his technical help.

References

[1] Y. Yang, K. Raipala, L. Holappa, Ironmaking, in: Treatise on Process Metallurgy, Elsevier, 2014, pp. 2–88.
[2] EUROSLAG, Granulated blastfurnace slag. Technical leaflet No. 1 2005, Available from: https://www.euroslag.com/wp-content/uploads/2018/12/LeafletGBS.pdf.
[3] FEhS, Hüttensand Datei, 2016.
[4] ACI, Slag cement in concrete and mortar, in: ACI Committee 233 Report, American Concrete Institute, 2003.
[5] E. Özbay, M. Erdemir, H.İ. Durmuş, Utilization and efficiency of ground granulated blast furnace slag on concrete properties–A review, Construct. Build. Mater. 105 (2016) 423–434.
[6] Services, A.S.M. 20x10mm concrete aggregate, Available from, http://www.asms.com.au/applications/20x10mm-concrete-aggregate, 2009.

[7] G. Mußgnug, Beitrag zur Frage der Mahlbarkeit von Hochofenschlacken (Zementschlacken) und Klinkern, Zement 31 (1942) 183–193.
[8] T. Jiang, et al., Effects of basicity and MgO in slag on the behaviors of smelting vanadium titanomagnetite in the direct reduction-electric furnace process, Metals 6 (5) (2016) 107.
[9] F. Shen, et al., Proper MgO/Al2O3 ratio in blast-furnace slag: analysis of proper MgO/Al2O3 ratio based on observed data, Metals 10 (6) (2020) 784.
[10] Yu Zhang, S. Karthikeyan, Ç. Oğuzhan, Microanalysis of unhydrated blast furnace slag grains in field concrete with different service life, Microsc. Microanal. (2022) 1–11.
[11] K. Mills, et al., A review of the factors affecting the thermophysical properties of silicate slags, High Temp. Mater. Process. 31 (4–5) (2012) 301–321.
[12] K.C. Mills, The influence of structure on the physico-chemical properties of slags, ISIJ Int. 33 (1) (1993) 148–155.
[13] S. Zhang, et al., Relationship between structure and viscosity of CaO–SiO2–Al2O3–MgO–TiO2 slag, J. Non-Cryst. Solids 402 (2014) 214–222.
[14] W. Xuan, et al., The influence of MgO on the crystallization characteristics of synthetic coal slags, Fuel 222 (2018) 523–528.
[15] S. Nie, et al., Impact of Mg substitution on the structure and pozzolanic reactivity of calcium aluminosilicate (CaO-Al2O3-SiO2) glasses, Cement Concr. Res. 138 (2020), 106231.
[16] Y. Zhang, et al., The effect of slag chemistry on the reactivity of synthetic and commercial slags, Construct. Build. Mater. 335 (2022), 127493.
[17] E. Douglas, A. Bilodeau, V. Malhotra, Properties and durability of alkali-activated slag concrete, Mater. J. 89 (5) (1992) 509–516.
[18] M.B. Haha, et al., Influence of slag chemistry on the hydration of alkali-activated blast-furnace slag — Part I: effect of MgO, Cement Concr. Res. 41 (9) (2011) 955–963.
[19] B. Walkley, et al., Structural evolution of synthetic alkali-activated CaO-MgO-Na2O-Al2O3-SiO2 materials is influenced by Mg content, Cement Concr. Res. 99 (2017) 155–171.
[20] K. Gong, C.E. White, Impact of chemical variability of ground granulated blast-furnace slag on the phase formation in alkali-activated slag pastes, Cement Concr. Res. 89 (2016) 310–319.
[21] S.A. Bernal, et al., MgO content of slag controls phase evolution and structural changes induced by accelerated carbonation in alkali-activated binders, Cement Concr. Res. 57 (2014) 33–43.
[22] S.M. Park, J. Jang, H.-K. Lee, Unlocking the role of MgO in the carbonation of alkali-activated slag cement, Inorg. Chem. Front. 5 (7) (2018) 1661–1670.
[23] S.Y. Wang, E. McCaslin, C.E. White, Effects of magnesium content and carbonation on the multiscale pore structure of alkali-activated slags, Cement Concr. Res. 130 (2020), 105979.
[24] T. Wagner, et al., GEM-Selektor geochemical modeling package: TSolMod library and data interface for multicomponent phase models, Can. Mineral. 50 (5) (2012) 1173–1195.
[25] D.A. Kulik, et al., GEM-Selektor geochemical modeling package: revised algorithm and GEMS3K numerical kernel for coupled simulation codes, Comput. Geosci. 17 (1) (2013) 1–24.
[26] W. Hummel, et al., Nagra Technical Report NTB 02-16, Wettingen, Switzerland, 2002.
[27] W. Hummel, et al., Nagra/PSI chemical thermodynamic data base 01/01, Radiochim. Acta 90 (9–11) (2002) 805–813.
[28] T. Matschei, et al., Thermodynamic properties of portland cement hydrates in the system CaO–Al2O3–SiO2–CaSO4–CaCO3–H2O, Cement Concr. Res. 37 (10) (2007) 1379–1410.
[29] B. Lothenbach, et al., Thermodynamic modelling of the effect of temperature on the hydration and porosity of Portland cement, Cement Concr. Res. 38 (1) (2008) 1–18.
[30] R.J. Myers, S.A. Bernal, J.L. Provis, A thermodynamic model for C-(N-) ASH gel: CNASH_ss. Derivation and validation, Cement Concr. Res. 66 (2014) 27–47.
[31] R.J. Myers, et al., Thermodynamic modelling of alkali-activated slag cements, Appl. Geochem. 61 (2015) 233–247.
[32] X. Ke, et al., Thermodynamic modelling of phase evolution in alkali-activated slag cements exposed to carbon dioxide, Cement Concr. Res. 136 (2020), 106158.
[33] S. Miyata, Anion-exchange properties of hydrotalcite-like compounds, Clay Clay Miner. 31 (4) (1983) 305–311.
[34] M. Thiery, et al., Investigation of the carbonation front shape on cementitious materials: effects of the chemical kinetics, Cement Concr. Res. 37 (7) (2007) 1047–1058.
[35] G. Villain, M. Thiery, G. Platret, Measurement methods of carbonation profiles in concrete: thermogravimetry, chemical analysis and gammadensimetry, Cement Concr. Res. 37 (8) (2007) 1182–1192.
[36] A. Morandeau, M. Thiery, P. Dangla, Investigation of the carbonation mechanism of CH and CSH in terms of kinetics, microstructure changes and moisture properties, Cement Concr. Res. 56 (2014) 153–170.
[37] F. Georget, et al., Stability of hemicarbonate under cement paste-like conditions, Cement Concr. Res. 153 (2022), 106692.
[38] Y. Zhang, O. Çopuroğlu, The role of hydrotalcite-like phase and monosulfate in slag cement paste during atmospheric and accelerated carbonation, Cement Concr. Compos. 132 (2022), 104642.
[39] M. Zajac, et al., CO2 mineralisation of Portland cement: towards understanding the mechanisms of enforced carbonation, J. CO2 Util. 38 (2020) 398–415.
[40] L. Black, et al., Structural features of C–S–H (I) and its carbonation in air—a Raman spectroscopic study. Part II: carbonated phases, J. Am. Ceram. Soc. 90 (3) (2007) 908–917.
[41] E.T. Stepkowska, et al., Calcite, vaterite and aragonite forming on cement hydration from liquid and gaseous phase, J. Therm. Anal. Calorim. 73 (1) (2003) 247–269.
[42] P.H. Borges, et al., Carbonation of CH and C–S–H in composite cement pastes containing high amounts of BFS, Cement Concr. Res. 40 (2) (2010) 284–292.
[43] P. Yu, et al., Structure of calcium silicate hydrate (C-S-H): near-, Mid-, and Far-infrared spectroscopy, J. Am. Ceram. Soc. 82 (3) (1999) 742–748.
[44] B.O. Mysen, et al., The influence of TiO2 on the structure and derivative properties of silicate melts, Am. Mineral. 65 (11–12) (1980) 1150–1165.
[45] Y. Sun, et al., FTIR, Raman and NMR investigation of CaO–SiO2–P2O5 and CaO–SiO2–TiO2–P2O5 glasses, J. Non-Cryst. Solids 420 (2015) 26–33.
[46] G.-H. Kim, I. Sohn, Effect of Al2O3 on the viscosity and structure of calcium silicate-based melts containing Na2O and CaF2, J. Non-Cryst. Solids 358 (12–13) (2012) 1530–1537.
[47] S.-M. Han, et al., Surface kinetics of nitrogen dissolution and its correlation to the slag structure in the CaO–SiO2, CaO–Al2O3, and CaO–SiO2–Al2O3 slag system, J. Non-Cryst. Solids 357 (15) (2011) 2868–2875.
[48] Y. Okada, et al., Relationship between NMR 29 Si chemical shifts and FT-IR wave numbers in calcium silicates, in: Nuclear Magnetic Resonance Spectroscopy of Cement-Based Materials, Springer, 1998, pp. 69–78.
[49] W. Ashraf, J. Olek, Carbonation behavior of hydraulic and non-hydraulic calcium silicates: potential of utilizing low-lime calcium silicates in cement-based materials, J. Mater. Sci. 51 (13) (2016) 6173–6191.
[50] M. Zajac, et al., Kinetics of enforced carbonation of cement paste, Cement Concr. Res. 131 (2020), 106013.
[51] G. Rimmelé, et al., Heterogeneous porosity distribution in Portland cement exposed to CO2-rich fluids, Cement Concr. Res. 38 (8–9) (2008) 1038–1048.
[52] S. Mindess, J.F. Young, D.J.E.C. Darwin, NJ, Concrete Prentice-Hall, 1981, p. 481.
[53] V. Ngala, C. Page, Effects of carbonation on pore structure and diffusional properties of hydrated cement pastes, Cement Concr. Res. 27 (7) (1997) 995–1007.
[54] M. Frías, S. Goñi, Accelerated carbonation effect on behaviour of ternary Portland cements, Compos. B Eng. 48 (2013) 122–128.
[55] B. Wu, G. Ye, Development of porosity of cement paste blended with supplementary cementitious materials after carbonation, Construct. Build. Mater. 145 (2017) 52–61.
[56] J.J. Chen, et al., Solubility and structure of calcium silicate hydrate, Cement Concr. Res. 34 (9) (2004) 1499–1519.
[57] V. Shah, et al., Changes in microstructure characteristics of cement paste on carbonation, Cement Concr. Res. 109 (2018) 184–197.
[58] I. Richardson, Tobermorite/jennite-and tobermorite/calcium hydroxide-based models for the structure of CSH: applicability to hardened pastes of tricalcium silicate, β-dicalcium silicate, Portland cement, and blends of Portland cement with blast-furnace slag, metakaolin, or silica fume, Cement Concr. Res. 34 (9) (2004) 1733–1777.
[59] R. Taylor, I. Richardson, R. Brydson, Composition and microstructure of 20-year-old ordinary Portland cement–ground granulated blast-furnace slag blends containing 0 to 100% slag, Cement Concr. Res. 40 (7) (2010) 971–983.
[60] J.-I. Escalante-Garcia, J. Sharp, The chemical composition and microstructure of hydration products in blended cements, Cement Concr. Compos. 26 (8) (2004) 967–976.
[61] S. Von Greve-Dierfeld, et al., Understanding the carbonation of concrete with supplementary cementitious materials: a critical review by RILEM TC 281-CCC, Mater. Struct. 53 (6) (2020) 1–34.
[62] T.F. Sevelsted, J. Skibsted, Carbonation of C–S–H and C–A–S–H samples studied by 13C, 27Al and 29Si MAS NMR spectroscopy, Cement Concr. Res. 71 (2015) 56–65.
[63] C.M. Bishop, Pattern recognition and machine learning, Springer 128 (9) (2006).
[64] G. Constantinides, F.-J. Ulm, K. Van Vliet, On the use of nanoindentation for cementitious materials, Mater. Struct. 36 (3) (2003) 191–196.
[65] G. Constantinides, F.J. Ulm, The effect of two types of CSH on the elasticity of cement-based materials: results from nanoindentation and micromechanical modeling, Cement Concr. Res. 34 (1) (2004) 67–80.
[66] G. Constantinides, F.-J. Ulm, The nanogranular nature of C–S–H, J. Mech. Phys. Solid. 55 (1) (2007) 64–90.
[67] D. Davydov, M. Jirasek, L. Kopecký, Critical aspects of nano-indentation technique in application to hardened cement paste, Cement Concr. Res. 41 (1) (2011) 20–29.
[68] M.L. Yu Zhang, Yidong Gan, Oğuzhan Çopuroğlu, Micro-mechanical Properties of Slag Rim Formed in Cement-Slag System Evaluated by Nanoindentation Combined with SEM. Under Review, 2022.
[69] B.J. Zhan, et al., Multi-scale investigation on mechanical behavior and microstructural alteration of CSH in carbonated Alite paste, Cement Concr. Res. 144 (2021), 106448.
[70] L. Mo, F. Zhang, M. Deng, Mechanical performance and microstructure of the calcium carbonate binders produced by carbonating steel slag paste under CO2 curing, Cement Concr. Res. 88 (2016) 217–226.
[71] X. Ouyang, et al., Understanding the adhesion mechanisms between CSH and fillers, Cement Concr. Res. 100 (2017) 275–283.
[72] P. Sulapha, et al., Carbonation of concrete containing mineral admixtures, J. Mater. Civ. Eng. 15 (2) (2003) 134–143.
[73] Y. Gao, et al., Effects of different mineral admixtures on carbonation resistance of lightweight aggregate concrete, Construct. Build. Mater. 43 (2013) 506–510.
[74] R. Bucher, et al., Service life of metakaolin-based concrete exposed to carbonation: comparison with blended cement containing fly ash, blast furnace slag and limestone filler, Cement Concr. Res. 99 (2017) 18–29.
[75] V. Shah, S. Bishnoi, Carbonation resistance of cements containing supplementary cementitious materials and its relation to various parameters of concrete, Construct. Build. Mater. 178 (2018) 219–232.

[76] O. Copuroglu, A. Fraaij, J. Bijen, Microstructural change of blast furnace slag cement paste due to carbonation, in: Application of Codes, Design and Regulations: Proceedings of the International Conference Held at the University of Dundee, Scotland, UK on 5–7 July 2005, Thomas Telford Publishing, 2005.
[77] E. Bernard, et al., Stability of hydrotalcite (Mg-Al layered double hydroxide) in presence of different anions, Cement Concr. Res. 152 (2022), 106674.
[78] G.G. Litvan, Variability of the nitrogen surface area of hydrated cement paste, Cement Concr. Res. 6 (1) (1976) 139–143.
[79] S. Walspurger, et al., High CO2 storage capacity in alkali-promoted hydrotalcite-based material: in situ detection of reversible formation of magnesium carbonate, Chem.–Eur. J. 16 (42) (2010) 12694–12700.
[80] P. Sahoo, et al., Rapid exchange between atmospheric CO2 and carbonate anion intercalated within magnesium rich layered double hydroxide, ACS Appl. Mater. Interfaces 6 (20) (2014) 18352–18359.
[81] L. Parrot, Prediction of cement hydration, in: Proceedings of the British Ceramic Society, 1984.